actuators

MDPI

Article

Variable Control Period Model Predictive Current Control with Current Hysteresis for Permanent Magnet Synchronous Motor Drives

Yuhao Guo [1], Fuxi Jiang [2], Siqi Wang [2], Shanmei Cheng [2] and Zuoqi Hu [1,*]

[1] School of Integrated Circuits, Huazhong University of Science and Technology, Wuhan 430074, China; yhguo2020@hust.edu.cn
[2] School of Artificial Intelligence and Automation, Huazhong University of Science and Technology, Wuhan 430074, China; fx_jiang@hust.edu.cn (F.J.); sqwang_hust@hust.edu.cn (S.W.); chengsm@hust.edu.cn (S.C.)
* Correspondence: hu_zuoqi@hust.edu.cn

Abstract

Conventional finite control set model predictive control (FCS-MPC) for permanent magnet synchronous motor (PMSM) drives suffers from a fundamental trade-off: shortening the control period improves current tracking but increases switching frequency and losses. This paper proposes a hysteresis-based variable control period MPC (HBVCP-MPC) to break this compromise. Unlike methods like direct torque control (DTC) and model predictive direct torque control (MPDTC) that use hysteresis to select voltage vectors (VV), our approach first selects the optimal VV via a cost function that balances current tracking accuracy and switching frequency. Hysteresis on the *dq*-axis currents is then employed solely to dynamically determine the application time of this pre-selected VV, which defines the variable control period. This grants continuous adjustment over the VV duration, enabling superior current tracking without a proportional rise in switching frequency. Experimental results confirm that the proposed method achieves enhanced steady-state performance at a comparable switching frequency.

Keywords: variable control period; model predictive current control (MPCC); permanent magnet synchronous motor (PMSM); current hysteresis

check for updates

Academic Editor: Paolo Mercorelli

Received: 28 September 2025
Revised: 21 October 2025
Accepted: 23 October 2025
Published: 25 October 2025

Citation: Guo, Y.; Jiang, F.; Wang, S.; Cheng, S.; Hu, Z. Variable Control Period Model Predictive Current Control with Current Hysteresis for Permanent Magnet Synchronous Motor Drives. *Actuators* **2025**, *14*, 517. https://doi.org/10.3390/act14110517

Copyright: © 2025 by the authors. Licensee MDPI, Basel, Switzerland. This article is an open access article distributed under the terms and conditions of the Creative Commons Attribution (CC BY) license (https://creativecommons.org/licenses/by/4.0/).

1. Introduction

Permanent magnet synchronous motors (PMSMs) are widely applied in industrial fields such as high-performance servo systems, electric vehicles, and wind power, due to their advantages of simple structure, high power density and high efficiency [1]. Meanwhile, the model predictive control (MPC) technique combined with the PMSM drive system has a certain potential for practical applications, and it has been extensively investigated [2,3]. Based on the waveform generation of the inverter, MPC applied to PMSM can be categorized into two types: modulated and non-modulated [4,5]. A considerable amount of modulated MPC strategies have been proposed to promote the performance of the PMSM system [6–9]. Meanwhile, the elimination of the modulation stage is becoming more and more attractive in recent years [10–14], and finite control set (FCS) MPC falls within this category.

In traditional FCS-MPC, a finite set of voltage vectors (VVs) are constructed based on the inverter's switching states. At a fixed control frequency, the optimal VV is selected from

this set and held for the entire control period. The removal of the intermediate modulation offers greater flexibility to tackle multiobjective control problems and provides a framework in which multiphase or multilevel control systems are more easily designed [11]. However, FCS-MPC faces the issue of variable switching frequency. And a more significant challenge of FCS-MPC is its large fluctuations in current and torque [15]. Since the VVs are discrete and are applied for fixed durations, fluctuations in current and torque are inevitable during reference tracking [16,17]. An increase in control frequency can help reduce these fluctuations, which also implies higher switching frequencies and losses. Moreover, the upper limit of the switching frequency is constrained by the switching devices, and a higher switching frequency also compresses the available calculation time.

To suppress current fluctuation and improve steady-state performance, the multivector MPC method has been introduced in [18–21]. Once the optimal VV is determined, it is combined with the adjacent vector by calculating the duty cycle, which allocates the time proportion of each vector within a control period. Another approach to reduce fluctuations is to expand the number of the candidate VVs. This can be achieved by incorporating predefined virtual vectors into the control set, as presented in [10,22]. Virtual vectors are essentially averaged VVs generated by combining multiple switching states. This method synthesizes the desired VV by combining the discrete VVs within a fixed period, allowing the current or torque to more precisely track the reference target by the end. However, it is clear that both of these approaches result in an increased number of VV transitions.

To mitigate fluctuations without increasing switching frequency, a variable switching point (VSP)-based predictive torque control strategy is introduced in [23,24]. This method enforces a single voltage switching event per control cycle while liberating the switching instant from conventional end-of-cycle constraints; extra flexibility in bridging the tail vector and head vector reduces the torque tracking error at the termination of the control period. Additionally, a variable action period (VAP) technology in FCS-MPC is proposed in [25,26], where the selection of the optimal VV is no longer based on tracking the reference target at fixed time intervals. And the action period of the selected VV is regulated to achieve the closest trajectory to the lead-pursuit direction. The implementation of VSP and VAP technologies significantly enhances tracking accuracy at specific time points. However, after transient alignment with reference targets, controlled variables inevitably diverge progressively from the reference trajectory due to finite voltage resolution; then, the overall operational behavior cannot be fully represented by the tracking performance at some instants.

A model predictive direct torque control (MPDTC), utilizing online optimization of switching sequences to keep the controlled variables in certain ranges while minimizing the switching frequency of the inverter, is described in [27]. The number of time steps is regulated for each VV in the switching sequence to maintain the predicted trajectories of torque and flux within their hysteresis bounds [28]. Meanwhile, the length of a single step should be well designed; as a rule of thumb, the sampling frequency f_s should be about two orders of magnitude higher than the switching frequency [14], to ensure a fine *granularity of switching* (the ratio between the sampling frequency and the switching frequency). For converters operating at high switching frequencies, more research effort should be paid.

Inspired by the aforementioned works, a hysteresis-based variable control period model predictive current control (HBVCP-MPCC) scheme is designed to regulate the control period length of the optimal VV with a continuous adjustment range. The core idea is to dynamically adjust the applying duration of the optimal VV, addressing the classic trade-off between current fluctuations (improved by shorter periods) and switching losses (improved by longer periods). The optimal VV can be determined based on the

reference voltages with a light computational burden, and the control period of VVs is dynamically regulated to keep the current within the hysteresis boundaries; moreover, the quantitative relationships of hysteresis bound width, motor parameters, and the allowable control period range are analyzed and validated.

The paper is organized as follows: Section 2 presents the PMSM system's mathematical model and discrete current prediction equations. Section 3 analyzes current fluctuations in traditional FCS-MPCC and proposes a variable control period algorithm to minimize fluctuations. Section 4 describes the implementation of HBVCP-MPCC, while Section 5 presents experimental results on a three-phase PMSM system. The conclusion is provided at the end.

2. Mathematical Models of PMSM

The dynamical model of the PMSM in the synchronous rotating frame can be expressed as follows:

$$\begin{cases} \dot{i}_d = \dfrac{1}{L_d}[u_d - R_s i_d + \omega_e L_q i_q] \\ \dot{i}_q = \dfrac{1}{L_q}[u_q - R_s i_q - \omega_e (L_d i_q + \varphi_m)], \end{cases} \tag{1}$$

where L_d and L_q are the q-axis inductance and d-axis inductance, R_s is the per-phase stator resistance, φ_m is the magnetic flux of the rotor, ω_e is the equivalent electrical angular velocity, i_d and i_q represent the d-axis and q-axis stator currents, and u_d and u_q are the d-axis and q-axis stator voltages.

A surface-mounted PMSM (SPMSM) is used to implement and validate the proposed method. Due to the approximately equal d-axis and q-axis inductances (i.e., $L_d \approx L_q$), they are denoted uniformly as the per-phase stator inductance L_s for simplicity. To facilitate the subsequent discussion, complex vectors are adopted to represent electrical variables with subscript dq. For example, the stator voltage is defined as $u_{dq} = u_d + ju_q$. Similarly, i_{dq} represents the stator current. So (1) is rewritten as

$$\dot{i}_{dq} = \frac{1}{L_s}[u_{dq} - R_s i_{dq} - j\omega_e \varphi_{dq}], \tag{2}$$

where φ_{dq} denotes the amplitude of magnet flux, expressed as

$$\varphi_{dq} = L_s i_{dq} + \varphi_m. \tag{3}$$

A discrete current prediction can be derived using a first-order Taylor series expansion with a sampling period T_s as

$$\hat{i}_{dq}(k+1) = i_{dq}(k) + \frac{T_s}{L_s}[u_{dq}(k) - R_s i_{dq}(k) - j\omega_e \varphi_{dq}(k)]. \tag{4}$$

Specifically, $i_{dq}(k)$ represents the measured current at the beginning of the kth period, while $u_{dq}(k)$ denotes the voltage applied during this period. The predictive current at the end of the period is given by $\hat{i}_{dq}(k+1)$.

And the predicted changing rate of dq-axis currents in the kth control period, denoted as $\hat{m}_{dq}(k)$, is defined as

$$\hat{m}_{dq}(k) = \frac{1}{L_s}[\hat{i}_{dq}(k+1) - i_{dq}(k)] = \frac{1}{L_s}[u_{dq}(k) - R_s i_{dq}(k) - j\omega_e \varphi_{dq}(k)] \tag{5}$$

In the subsequent analysis, it is assumed that $\hat{m}_{dq}(k)$ remains constant during a single control period when the inverter switching state is unchanged, as illustrated in [23]. And this assumption holds under the following conditions:

(1) Magnetic Saturation: Magnetic saturation is assumed to have negligible influence. If the PMSM exhibits noticeable saturation, the model in (1) must be refined.

(2) Rotation Angle: The electrical rotational angle θ_e is assumed constant during T_s. However, at extreme high electrical speeds, this assumption may be violated. For instance, at an electrical speed of 30,000 rpm, a sampling period T_s of 100 µs would result in a change of 0.1π rad to θ_e.

(3) Time-Varying Parameters: The time constants of the non-linear time-varying parameters, such as the electrical angular velocity ω_e, stator resistance R_s, rotor magnetic flux φ_m and stator phase inductance L_s, are significantly larger than the sampling period T_s. Therefore, their variations do not appreciably affect the changing rate of current over a control period.

3. Comparison of the Conventional FCS-MPCC and the Proposed HBVCP-MPCC

3.1. Conventional FCS-MPCC

For a two-level three-phase voltage source inverter, six non-zero VVs ($V1 \sim V6$) and two zero VVs ($V0$ and $V7$) can be generated. Each of these VVs, represented as $u_{dq}(k)$, yields the corresponding predicted current $\hat{i}_{dq}(k+1)$ by (4), as illustrated in Figure 1. In this figure, the round point i^*_{dq} represents the current reference; assuming a constant rate of current change, the red lines originating from the square point $i_{dq}(k)$ depict the possible trajectories of current evolution, driven by the applied VVs.

When the conventional FCS-MPC is adopted to achieve current control for PMSMs, the deadbeat method is usually applied, and it forces the prediction $\hat{i}_{dq}$ to approach the reference i^*_{dq} at the end of each period. For the example shown in Figure 1, The current trajectory under $V1$ represented by a red solid line achieves the minimum tracking error marked as the green line, and the suboptimal trajectories are represented by the red dashed lines. Actually, due to the delay compensation in PMSM-driven systems, this $V1$ is determined in the previous $(k-1)$th period, allowing it to be applied at the beginning of the kth period.

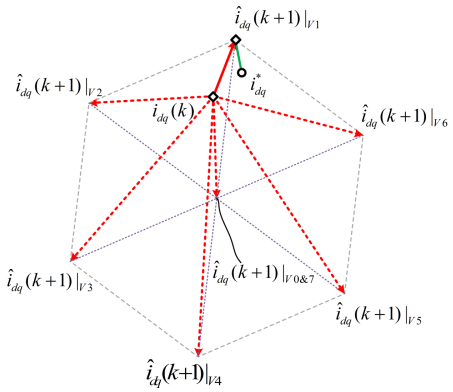


Figure 1. Predicted stator current trajectory under FCS-MPCC during the kth interval.

In the kth period, the focus is to select out the optimal VV for the next period. To this end, the predicted current $\hat{i}_{dq}(k+2)$ at the end of the $(k+1)$th period should be predicted by

$$\hat{i}_{dq}(k+2) = \hat{i}_{dq}(k+1) + \frac{T_s}{L_s}[u_{dq}(k+1) - R_s\hat{i}_{dq}(k+1) - j\omega_e\hat{\varphi}_{dq}(k+1)]. \quad (6)$$

As illustrated in Figure 2, the predicted current reaches the square point $\hat{i}_{dq}(k+1)$ at the end of the kth period, and the blue-dashed circle is used to indicate the fluctuation range of

the current. Subsequently, all possible VVs yield seven distinct predictions for $\hat{i}_{dq}(k+2)$. A cost function quantifying the tracking error for each candidate VV is then constructed as

$$g = \left| i_{dq}^{*} - \hat{i}_{dq}(k+2) \right|. \tag{7}$$

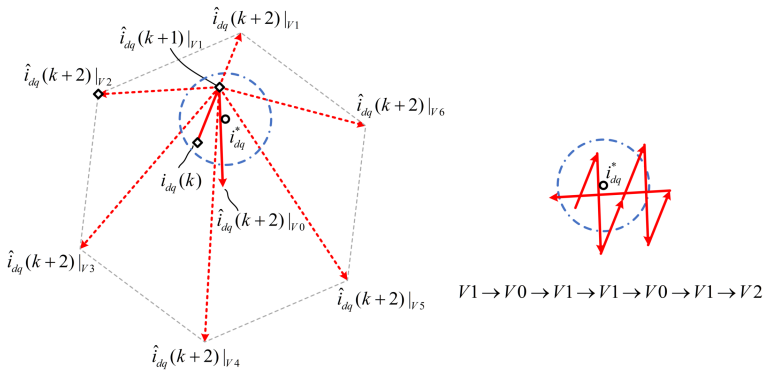


Figure 2. Predicted stator current trajectory under FCS-MPCC.

For the state shown in Figure 2, the prediction corresponding to the zero VV minimizes g in (7), indicating the smallest tracking error. Consequently, the zero VV is selected as the optimal VV for the $(k+1)$th control period. Figure 2 also presents the current trajectories resulting from recursively applying this prediction method over a long prediction horizon. For convenience in expression, the minor changes in current gradients between adjacent control periods are neglected in Figures 1 and 2.

It is clear that the steady-state performance can be improved by adopting a reduced T_s. However, this results in a higher switching frequency and increased switching losses.

3.2. Proposed HBVCP-MPCC

In conventional FCS-MPCC, the optimal VV is selected based on the tracking error between the predicted current $\hat{i}_{dq}$ and its reference at fixed sampling instants (i.e., kT_s, $(k+1)T_s$), with switching of the VVs also occurring at these points. As a result, the application duration for VVs is limited to T_s or its integer multiples. Under these constraints, FCS-MPCC ensures tracking of the reference; however, it may lead to larger current fluctuations over the entire control process.

Figure 3 illustrates how the proposed HBVCP-MPCC reduces current fluctuations in the q-axis over several consecutive control periods. As demonstrated in the case of HBVCP-MPCC, the VV remains unchanged as long as the currents (both the d-axis and q-axis currents) stay within their defined hysteresis width $2h$. And the switching sequence employed by HBVCP-MPCC is similar to that of FCS-MPCC, with the main difference being the shift in the switching points. It implies that the switching frequencies of both methods are approximately the same; however, HBVCP-MPCC achieves a much smaller range of current fluctuation. Figure 4 depicts the current trajectory under the proposed HBVCP method. By adjusting the action duration of the VVs rather than fixing it to T_s or its integer multiples, the current trajectories can be flexibly constrained within the blue-dashed circle, proving that the additional control freedom provided by variable control period (VCP) is able to improve the reference tracking behavior without relying on increasing the switching frequency.

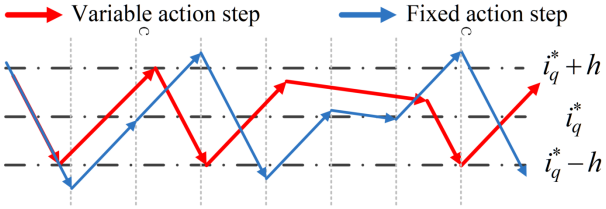


Figure 3. Current fluctuations under different control strategies.

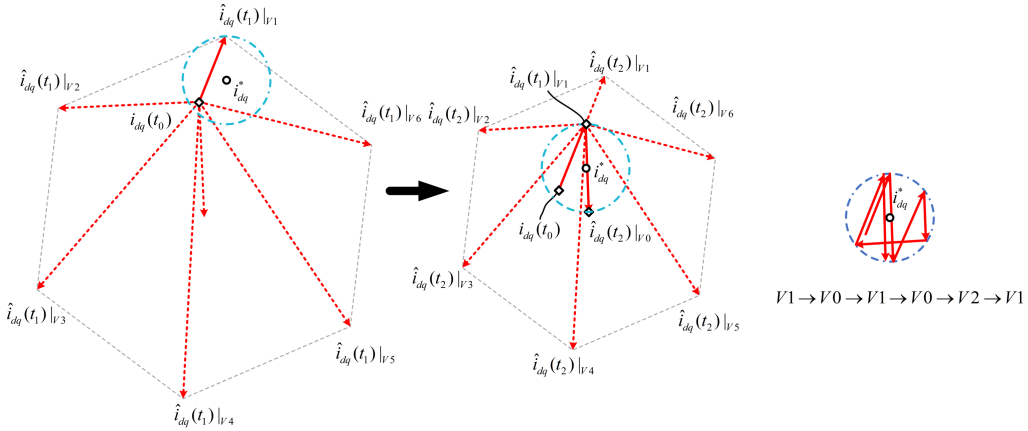


Figure 4. Predicted stator current trajectory with proposed HBVCP-MPCC.

4. Implementation of Predictive Current Control with Variable Control Period

This section presents the implementation process of HBVCP-MPCC. Firstly, a cost function considering the variation range of the reference voltage is utilized to select the optimal VV. Subsequently, its application duration is adjusted by the current hysteresis, allowing for variability in the control period. The control scheme of HBVCP-MPCC is illustrated in Figure 5.

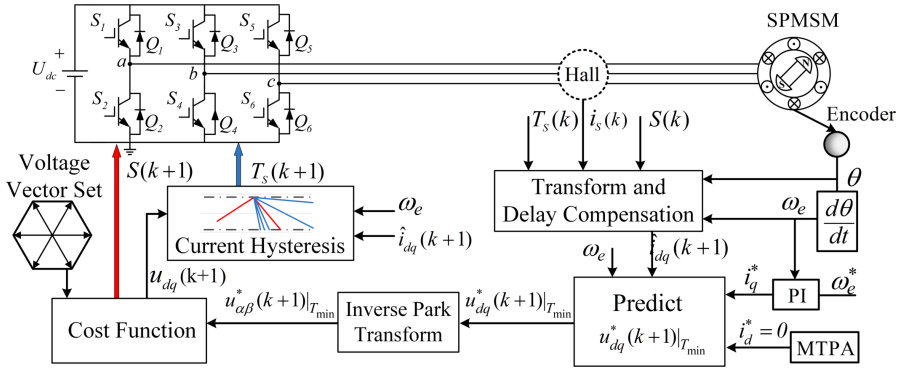


Figure 5. Block diagram of the proposed HBVCP-MPCC.

In the prediction process, the predicted duration of the optimal VV is configured as the length of the next control period. To simplify the implementation process, a non-uniform sampling method is employed to accommodate the variable control period length, with the sampling interval synchronized to the variable control period. It means that sampling occurs at the end of each control period. A typical example of the switching schematic diagram is depicted in Figure 6. In the kth control period, the switching state $S(k)$ of the inverter is updated at the beginning, i.e., time t_0; meanwhile, the phase currents and the rotating position are sampled. $S(k)$ remains active for the duration $T_s(k)$ until time t_1, during which the inverter's state $S(k+1)$ for the next control period is computed, along with its corresponding duration period $T_s(k+1)$.

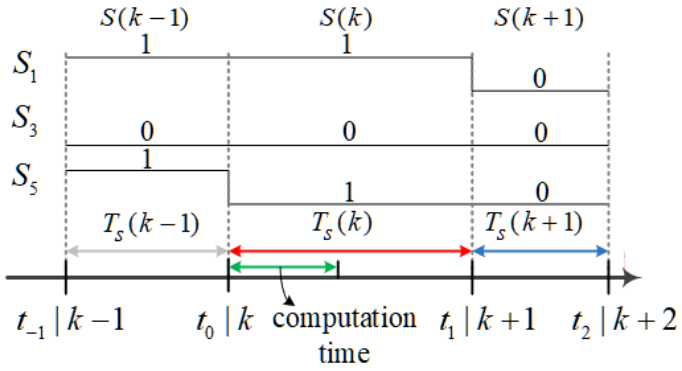


Figure 6. VV switching with non-uniform sampling.

Although the length of each control period varies, only one VV is executed between two sampling points, eliminating the need for complex duty cycle settings. The predicted current at the $(k+1)$th sampling point can be simply expressed as

$$\hat{i}_{dq}(k+1) = i_{dq}(k) + \frac{T_s(k)}{L_s}[u_{dq}(k) - R_s i_{dq}(k) - j\omega_e \varphi_{dq}(k)]. \tag{8}$$

For clarity and to distinguish from the fixed sampling case, the duration of the kth control period is denoted as $T_s(k)$ in the VCP method. Then the prediction process of $\hat{i}_{dq}(k+2)$ in (6) should also be rewritten as

$$\hat{i}_{dq}(k+2) = \hat{i}_{dq}(k+1) + \frac{T_s(k+1)}{L_s}[u_{dq}(k+1) - R_s \hat{i}_{dq}(k+1) - j\omega_e \hat{\varphi}_{dq}(k+1)]. \tag{9}$$

4.1. Width of Current Hysteresis and Range of Control Period

The range of the VCP is defined based on the fundamental parameters of the motor and the control requirements. In the kth control period with a VCP of $T_s(k)$, there exists a reference voltage $u^*_{dq}(k)$ that satisfies the following conditions:

$$i^*_{dq} = i_{dq}(k) + \frac{T_s(k)}{L_s}[u^*_{dq}(k) - R_s i_{dq}(k) - j\omega_e \varphi_{dq}(k)]. \tag{10}$$

According to (8), the current tracking error $\Delta i_{dq}(k)$ between $\hat{i}_{dq}(k+1)$ and i^*_{dq} can be calculated by

$$\Delta i_{dq}(k+1) = \frac{T_s(k)}{L_s}[u_{dq}(k) - u^*_{dq}(k)]. \tag{11}$$

When the difference $\Delta u_{dq}(k)$ between $u_{dq}(k)$ and $u^*_{dq}(k)$ becomes smaller, $\Delta i_{dq}(k+1)$ will also become smaller.

As illustrated in Figure 7, $u^*_{dq}(k)$ is located in the vicinity of V_2, indicating that V_2 is selected as $u_{dq}(k)$. During the long-term operation of the motor, and assuming that there is no significant over-modulation, the red arrow's landing point indicates the possible location of $u^*_{dq}(k)$. The $u^*_{dq}(k)$ that maximizes $|\Delta u_{dq}(k)|$ is represented by the red solid line, and the length of the corresponding green solid line can be used to calculate the maximum $|\Delta u_{dq}(k)|$, $|\Delta u_{dq}(k)|_{max}$, as

$$\left|\Delta u_{dq}(k)\right|_{max} = \frac{2\sqrt{3}}{9} U_{dc}, \tag{12}$$

where U_{dc} is DC link voltage in Figure 5, and the coefficient is derived from the equal-amplitude Clark transformation. As for the $u^*_{dq}(k)$ falling near other VVs, the situation can be the same, and the range of $|\Delta i_{dq}(k+1)|$ under $T_s(k)$ can be confined by (11) and (12):

$$\left|\Delta i_{dq}(k+1)\right| \in [0, \frac{2\sqrt{3}}{9L_s} T_s(k) U_{dc}]. \tag{13}$$

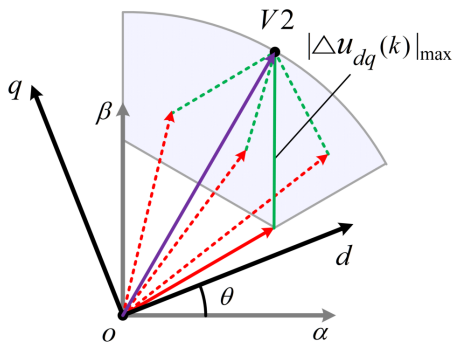


Figure 7. Reference voltage near $V2$.

Since $T_s(k)$ can be continuously adjusted within the VCP range, where the minimum is T_{min}, $|\Delta i_{dq}(k+1)|$ can be further constrained within

$$\left|\Delta i_{dq}(k+1)\right| \in [0, \frac{2\sqrt{3}}{9L_s} T_{min} U_{dc}]. \tag{14}$$

When distance from the hysteresis center to the upper or lower boundary is set to h according to the application requirement, it should be ensured that h cannot be exceeded by the maximum of $|\Delta i_{dq}(k+1)|$. Meanwhile, T_{min} should be as large as possible to reduce the switching frequency so that

$$h = \frac{2\sqrt{3}}{9L_s} T_{min} U_{dc}. \tag{15}$$

Regarding the maximum control period length T_{max}, if it is too small, it will fail to effectively reduce the switching frequency. Conversely, if T_{max} is too large, the accuracy of the predictive model may deteriorate. As described by (5), when the optimal VV results in $\hat{m}_{dq}(k) = 0$ and the measured current is near its reference i^*_{dq}, the relative position between the predicted current and i^*_{dq} remains constant for an extended period. This conclusion, however, is based on the assumption that the change in the motor's rotational angle is negligible. As illustrated in Figure 8, if T_{max} is long enough to allow for a significant change in the rotation angle, the dq frame will undergo a substantial rotation relative to the $\alpha\beta$ frame, to a new position, $d'q'$. Consequently, the reference current i^*_{dq}, defined in the dq-axis, will also rotate accordingly. ${i^*_{dq}}'$ in dq-axis can be obtained by applying a rotational transformation to i^*_{dq} as

$${i^*_{dq}}' = i^*_{dq} e^{j\omega_e T_{max}}. \tag{16}$$

The error between i^*_{dq} and ${i^*_{dq}}'$ should first meet,

$$\left|{i^*_{dq}}' - i^*_{dq}\right| < h. \tag{17}$$

By substituting (15) and (16) into (17), the following is obtained:

$$\left|i^*_{dq}(1 - e^{j\omega_e T_{max}})\right| = 2\left|i^*_{dq}\right| sin(\frac{\omega_e T_{max}}{2}) < \frac{2\sqrt{3}}{9L_s} T_{min} U_{dc}. \tag{18}$$

Generally, T_{max} can be initially estimated by (18) and then determined through specific experiments.

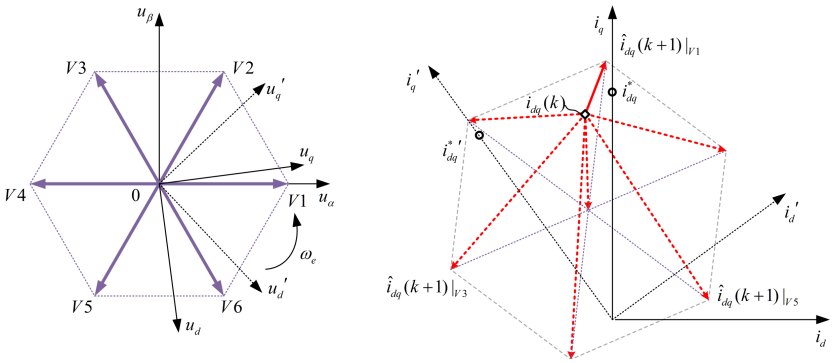


Figure 8. Change in the rotation angle.

4.2. Determination of Optimal VV

The optimal VV selection process becomes more complex with the application of VCP technology. As demonstrated in Figure 9, when all VVs are applied over a time interval of T_{min}, the current trajectories under $V1$ and $V6$ remain within a circle centered at i_{dq}^* with radius h, indicating that both $V1$ and $V6$ are viable candidates for the optimal VV selection. Then, a cost function g_1 is formulated to find out the candidate vectors like $V1$ and $V6$:

$$g_1 = \left| i_{dq}^* - \hat{i}_{dq}(k+2)|_{T_{min}} \right|, \quad g_1 < h, \tag{19}$$

where $\hat{i}_{dq}(k+2)|_{T_{min}}$ denotes the predicted current $\hat{i}_{dq}(k+2)$ in (9) with $T_s(k+1)$ euqal to T_{min}, and it is calculated by

$$\hat{i}_{dq}(k+2)|_{T_{min}} = \hat{i}_{dq}(k+1) + \frac{T_{min}}{L_s}[u_{dq}(k+1) - R_s\hat{i}_{dq}(k+1) - j\omega_e\hat{\varphi}_{dq}(k+1)]. \tag{20}$$

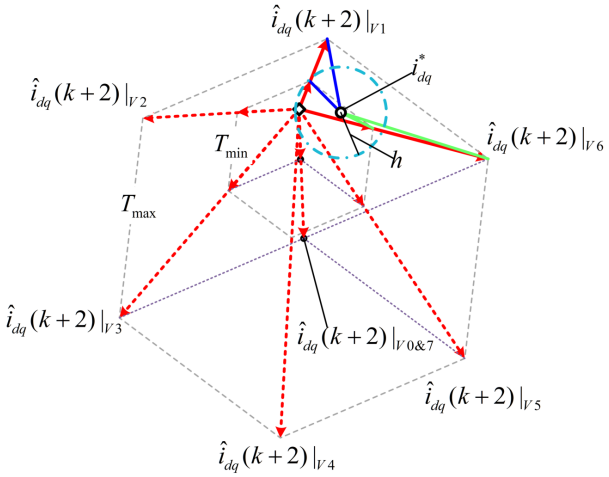


Figure 9. Tracking errors between the current trajectories and the current reference under different time scales.

For each discrete VV from $V0$ to $V7$, the corresponding $u_{dq}(k+1)$ is used in (20) to calculate a set of predicted currents, $\hat{i}_{dq}(k+2)|_{T_{min}}$. The optimal vector is then selected based on these currents: if no predicted current satisfies the constraint in (19), the VV corresponding to the predicted current that minimizes g_1 is chosen; if only one $\hat{i}_{dq}(k+2)|_{T_{min}}$ satisfies (19), its VV is selected directly; if multiple predictions meet (19), the VV associated with the fewest switching operations is the optimal vector.

In a three-phase two-level inverter, the optimal VV can be selected out via (19) with at most 7 iterations. However, as the voltage levels increase, the required number of iterations rises significantly. To simplify the above calculation process, a computationally efficient method based on reference voltage is adopted. First, according to (10) and (20), the reference voltage u_{dq}^{*} that ensures $\hat{i}_{dq}(k+2)|_{T_{min}}$ fully tracks i_{dq}^{*}, represented by $u_{dq}^{*}(k+1)|_{T_{min}}$, can be calculated as

$$u_{dq}^{*}(k+1)|_{T_{min}} = \frac{L_s}{T_{min}}[i_{dq}^{*} - \hat{i}_{dq}(k+1)] + R_s\hat{i}_{dq}(k+1) + j\omega_e\hat{\varphi}_{dq}(k+1). \tag{21}$$

Meanwhile, based on (20), $u_{dq}(k+1)$ should meet

$$u_{dq}(k+1) = \frac{L_s}{T_{min}}[\hat{i}_{dq}(k+2)|_{T_{min}} - \hat{i}_{dq}(k+1)] + R_s\hat{i}_{dq}(k+1) + j\omega_e\hat{\varphi}_{dq}(k+1). \tag{22}$$

Subtracting (21) with (22) yields

$$u_{dq}^{*}(k+1)|_{T_{min}} - u_{dq}(k+1) = \frac{L_s}{T_{min}}[i_{dq}^{*} - \hat{i}_{dq}(k+2)|_{T_{min}}]. \tag{23}$$

According to the relationship in (15), (19) and (23), the candidate $u_{dq}(k+1)$ must satisfy

$$\left|u_{dq}^{*}(k+1)|_{T_{min}} - u_{dq}(k+1)\right| < \frac{L_s}{T_{min}}h = \frac{2\sqrt{3}}{9}U_{dc}. \tag{24}$$

In the $\alpha\beta$ coordinate frame, (24) becomes more intuitive and clearer. With the inverse Park's transformation, $u_{\alpha\beta}^{*}(k+1)|_{T_{min}}$ and $u_{\alpha\beta}(k+1)$ are transformed from $u_{dq}^{*}(k+1)|_{T_{min}}$ and $u_{dq}(k+1)$, and they should also meet

$$\left|u_{\alpha\beta}^{*}(k+1)|_{T_{min}} - u_{\alpha\beta}(k+1)\right| < \frac{2\sqrt{3}}{9}U_{dc}. \tag{25}$$

As illustrated in Figure 10, the candidate VVs can initially be identified based on the sector in which $u_{\alpha\beta}^{*}(k+1)|_{T_{min}}$ is located, specifically, $V1$, $V6$ and the zero VVs. The sector containing $u_{\alpha\beta}^{*}(k+1)|_{T_{min}}$ can be directly determined from the angle $\theta_{\alpha\beta}$ in Figure 10. Subsequently, the candidate VVs are further narrowed down to $V1$ and $V6$ by (25). Following the previously described criteria, the VV that achieves the least switching operations will finally be chosen as the optimal VV. This method can be extended to multilevel inverter applications, and its computational complexity does not increase as the number of voltage levels grows.

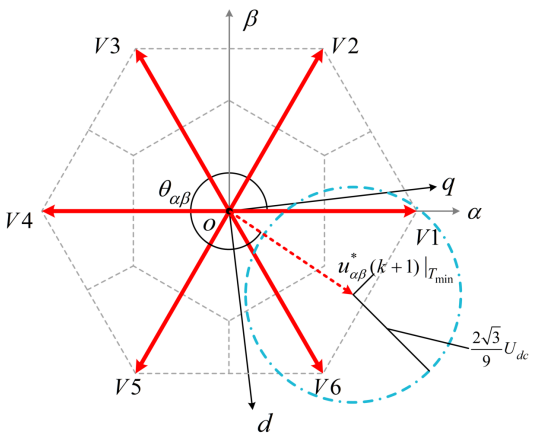


Figure 10. Evolution of the reference voltage over time.

4.3. Regulation of Optimal Control Period

After the optimal VV is determined, its duration is regulated by the current hysteresis. Although the hysteresis shape is circular in Figure 4, various additional hysteresis shapes have also been investigated in [29–31]. For the computational convenience in practical implementations, the shape is simplified to a rectangular form in the proposed HBVCP-MPCC. Consequently, the current hysteresis can be divided into two independent components in the d- and q-axis, as illustrated in Figure 11, with widths $2h_d$ and $2h_q$ based on (15). By (9), the predicted changing rate of the current in the $(k+1)$th control period can be considered constant and calculated by

$$\begin{cases} \hat{m}_d(k+1) = \dfrac{1}{L_d}[u_d(k+1) - R_s\hat{i}_d(k+1) + \omega_e\hat{\varphi}_q(k+1)] \\ \hat{m}_q(k+1) = \dfrac{1}{L_q}[u_q(k+1) - R_s\hat{i}_q(k+1) - \omega_e\hat{\varphi}_d(k+1)], \end{cases} \tag{26}$$

where $\hat{m}_d(k+1)$ and $\hat{m}_q(k+1)$ represent the changing rates of d- and q-axis currents during that period. And even in surface-mounted PMSMs, the d- and q-axis inductances differ slightly. To achieve more accurate and flexible control of the dq-axis currents, the inductances in (26) are therefore denoted separately as L_d and L_q.

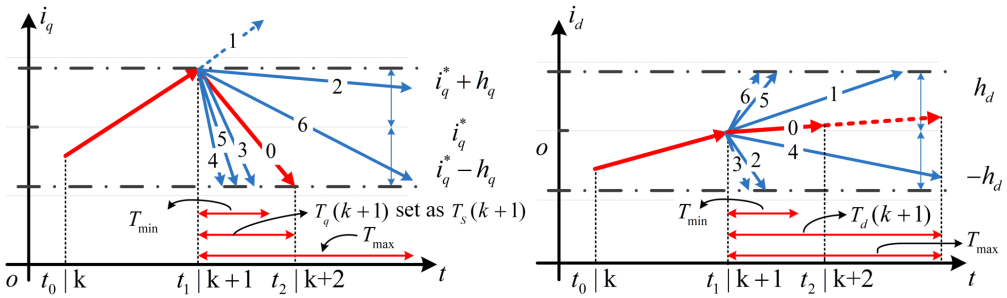


Figure 11. Regulating the control period. (**a**) With current hysteresis in q-axis. (**b**) With current hysteresis in d-axis.

Then, the regulated time when considering current in d-axis can be expressed as

$$T_d(k+1) = \begin{cases} \dfrac{i_d^* + h_d - \hat{i}_d(k+1)}{\hat{m}_d(k+1)}, & \hat{m}_d(k+1) > 0 \\ \dfrac{i_d^* - h_d - \hat{i}_d(k+1)}{\hat{m}_d(k+1)}, & \hat{m}_d(k+1) < 0. \end{cases} \tag{27}$$

Similarly, $T_q(k+1)$ can be calculated by the q-axis hysteresis. And to ensure that these two currents remain within their respective hysteresis, the regulated control period for the optimal VV is given by

$$T_s(k+1) = min\left[T_d(k+1), T_q(k+1)\right]. \tag{28}$$

5. Experimental Verification

A digital signal processor (DSP), TMS320F28335, is selected as the controller of the PMSM drive system to implement the proposed HBVCP-MPCC method. And the detailed setup of the experimental platform is presented in Figure 12. The dual PMSM coaxial drivetrain consists of two PMSMs with similar power ratings. One motor serves as the tested motor for evaluating the proposed control method, while the other works as a load torque generator. Parameters of the tested motor are listed in Table 1.

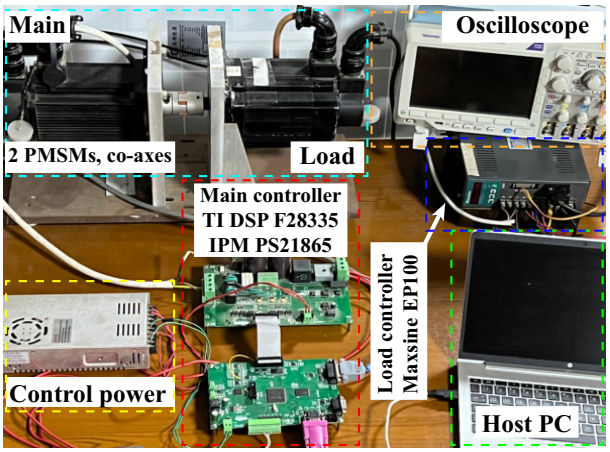


Figure 12. Experiment platform of the PMSM drive system.

Table 1. Parameters of the tested PMSM.

Parameters	Symbol	Value
Rated Power	P_N	1.6 kW
Pole Pairs	n_p	4
Inductance in Nameplate	L_s	1.515 mH
Tested Inductance in d-axis	L_d	1.4115 mH
Tested Inductance in q-axis	L_q	1.6313 mH
Stator Resistance	R_s	0.338 Ω
Magnet Flux Amp.	φ_m	0.1105 Wb
Rated Speed	n_N	3000 rpm
Rated Torque	T_N	6 Nm
Rated Current	I_N	8 A

It is noteworthy that, although this motor is surface-mounted with a stator inductance L_s of 1.515 mH in the nameplate, the measurements reveal that the d- and q-axis inductances are not identical, with L_d and L_q being 1.4115 mH and 1.6313 mH, respectively. Compared to the nameplate value, the deviations are both within 7%. Given this slight discrepancy, the conventional $i_d^* = 0$ is maintained for Maximum Torque Per Ampere (MTPA) operation to simplify the control strategy.

5.1. Steady-State Performance Comparison

To validate the ability of proposed HBVCP-MPCC in suppressing the current fluctuations, steady-state comparisons are experimentally conducted between proposed method and traditional FCS-MPCC.

Based on the DSP computation time and the switching frequency limitations of the inverter, T_{min} is set to 40 µs. When U_{dc} is set to 100 V, and in combination with the motor parameters listed in Table 1, the corresponding values for h_d and h_q are 1.09 A and 0.94 A, as given by (15), so the expected current fluctuation ranges in the d-axis and q-axis are 2.18 A and 1.88 A, respectively. Before the experiment begins, T_{max} should be determined firstly, and it can be set to a larger value initially, such as 5 to 10 times T_{min}, according to (18) and parameters in Table 1. Trial runs conducted at 1000 rpm reference speed and 2.25 Nm load reveal that each vector's control period is not longer than 4 times T_{min}, according to the ratios shown in Figure 13. It can also help to confirm the successful implementation of VCP. Under other operating conditions, the distribution of VCP remains consistent with Figure 13. Since there are no periods longer than 4 times T_{min}, T_{max} is set to $4T_{min}$ in the following experiments, i.e., 160 µs. Interestingly, it is observed that when the motor

operates in steady state, the average control period T_{avg} remains around 80 µs under various operating conditions. T_{avg} is given by

$$T_{avg} = \frac{1}{n}\sum_{k=1}^{n} T_s(k). \tag{29}$$

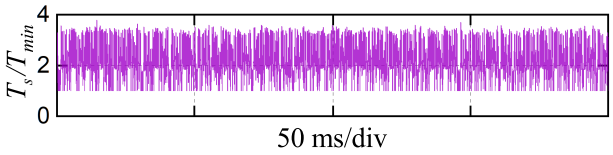


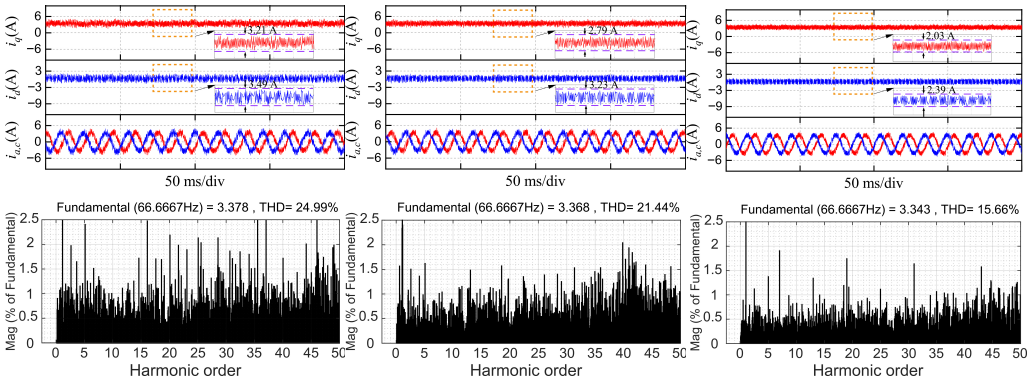
Figure 13. The ratio of each vector's application duration to T_{min}.

For a reasonable comparison, the sampling period of FCS-MPCC needs to be appropriately configured, and two values are, respectively, adopted in the FCS-MPCC experiment. One of the sampling periods in FCS-MPCC is set to 76 µs, which is slightly smaller than the T_{avg} in the proposed HBVCP-MPCC. And with the setting of 76 µs, the average switching frequencies of these two schemes remain nearly the same across most of the operating conditions, when the optimal VV of FCS-MPCC is simply determined by the cost function (7). However, it does not allow for high *granularity of switching* in FCS-MPCC [14], and it also means that the minimum allowable execution time for VVs differs between the two methods. Therefore, under a sampling period of 40 µs, additional experiments are conducted with FCS-MPCC, and constraints on voltage transitions are imposed to reduce its switching frequency to a level comparable to that of the proposed HBVCP-MPCC. Thus, when FCS-MPCC is conducted with a 40 µs sampling period, the cost function incorporates both current error and switching actions as

$$g_2 = \lambda|i_{dq}^{*} - \hat{i}_{dq}(k+2)| + (1-\lambda)N_{sw}(k+1), \tag{30}$$

where N_{sw} denotes the number of switching actions required to transition between the VVs in the kth and $(k+1)$th control periods.

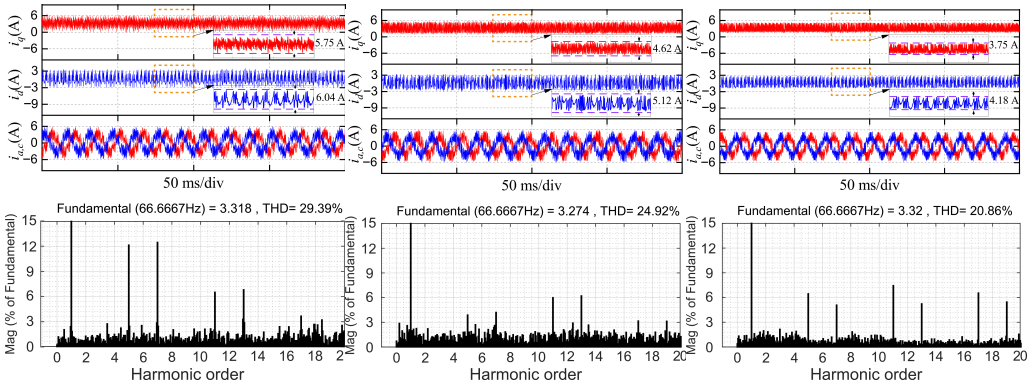
When the torque load is set to 2.25 Nm and the mechanical rotational speed remains at 1000 rpm, both the HBVCP-MPCC and the FCS-MPCC (with a 76 µs sampling period) exhibit comparable average switching frequencies of approximately 2 kHz. By adjusting the parameter λ in (30), the switching frequency of FCS-MPCC at a 40 µs sampling period is also brought close to this frequency. This approach will be adopted across all the operating conditions to maintain the same switching frequencies for these three control schemes. The corresponding experimental results, including phase A and C currents, dq-axis currents and the FFT analysis results (with maximum calculation frequency of 3.3 kHz) of phase A current, are presented in Figure 14. It can be observed that, although the switching frequencies of FCS-MPCCs with sampling periods of 76 µs and 40 µs are adjusted to be the same, higher *granularity of switching* with a 40 µs sampling period significantly improves the current fluctuations. Meanwhile, the fluctuation range of the proposed algorithm in the d-axis current is 2.39 A and the q-axis current fluctuates by 2.03 A. The measured values align with the predetermined hysteresis boundaries ($2h_d$ and $2h_q$ of 2.18 A and 1.88 A, respectively), well within acceptable experimental error margins, which validates the effectiveness of the proposed HBVCP-MPCC. Crucially, while maintaining a comparable switching frequency, the proposed algorithm exhibits significantly smaller current fluctuations and a lower THD compared to the other two FCS-MPCC strategies, underscoring its superior performance efficiency.



(**a**) (**b**) (**c**)

Figure 14. Steady-state waveforms of these control strategies with 100 V U_{dc}, 1000 rpm reference speed and 2.25 Nm load: q-axis current, d-axis current, phase A and phase C currents, and FFT analysis results of phase A current. (**a**) FCS-MPCC with a 76 μs sampling period. (**b**) FCS-MPCC with a 40 μs sampling period. (**c**) HBVCP-MPCC.

To validate the impact of the DC bus voltage on the hysteresis bound and to compare the performance of these algorithms under different operating conditions, DC bus voltage U_{dc} is increased from 100 V to 180 V while maintaining the same speed of 1000 rpm and a load of 2.25 Nm. According to (15), the values of $2h_d$ and $2h_q$ should also be 1.8 times, set to 4.0 A and 3.4 A, respectively. The relevant experimental data is presented in Figure 15. The data shown in the figure still demonstrates that the proposed method achieves the best performance. And the fluctuation ranges of the dq-axis currents with HBVCP-MPCC are 4.18 A and 3.75 A, matching to the setting of current hysteresis.



(**a**) (**b**) (**c**)

Figure 15. Steady-state waveforms of these control strategies with 180 V U_{dc}, 1000 rpm reference speed and 2.25 Nm load: q-axis current, d-axis current, phase A and phase C currents, and FFT analysis results of phase A current. (**a**) FCS-MPCC with a 76 μs sampling period. (**b**) FCS-MPCC with a 40 μs sampling period. (**c**) HBVCP-MPCC.

To verify the effectiveness of the proposed method under conditions close to the rated speed and rated load, the performance of the three methods is compared with a U_{dc} of 180 V, a reference speed of 2500 rpm, and a load of 4.5 Nm. As shown in Figure 16, the proposed method remains effective under high load and high speed conditions, with 4.45 A and 3.91 A fluctuations in dq-axis currents, respectively. In comparison, under 180 V DC bus voltage, 1000 rpm speed and 2.25 Nm load, the d-axis and q-axis current fluctuations for the proposed method are 4.18 A and 3.75 A in Figure 15. This indicates that current fluctuation ranges are less impacted by the changes in speed or load when FCS methods are adopted; it is because they are more affected by the discrete VVs. The experimental results

corresponding to Figures 14–16 are summarized in Table 2, where n_r is the mechanical rotational speed, T_l stands for the torque load, f_{sw} denotes the average switching frequency per inverter leg, and R_q and R_d are the current fluctuation ranges in the dq-axis.

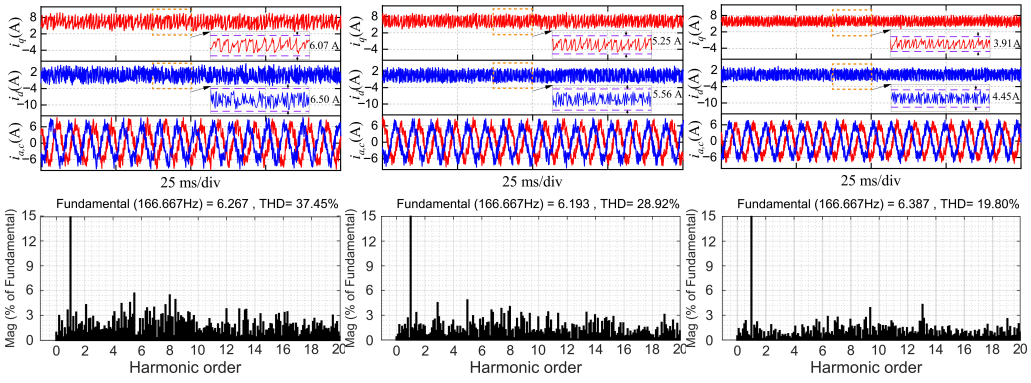


Figure 16. Steady-state waveforms of these control strategies with 180 V U_{dc}, 2500 rpm reference speed and 4.5 Nm load: q-axis current, d-axis current, phase A and phase C currents, and FFT analysis results of phase A current. (**a**) FCS-MPCC with a 76 µs sampling period. (**b**) FCS-MPCC with a 40 µs sampling period. (**c**) HBVCP-MPCC.

Table 2. Steady-state experimental results with three schemes adopted under different conditions.

Scheme	U_{dc} (V)	n_r (rpm)	T_l/T_N	f_{sw} (kHz)	R_q (A)	R_d (A)	THD
FCS-MPCC (76 µs)	100	1000	37.5%	1.99	3.21	3.49	24.99%
FCS-MPCC (40 µs)	100	1000	37.5%	1.98	2.79	3.23	21.44%
HBVCP-MPCC	100	1000	37.5%	2.01	2.03	2.39	15.66%
FCS-MPCC (76 µs)	180	1000	37.5%	2.05	5.75	6.04	46.67%
FCS-MPCC (40 µs)	180	1000	37.5%	2.05	4.62	5.12	43.31%
HBVCP-MPCC	180	1000	37.5%	2.09	3.75	4.18	35.24%
FCS-MPCC (76 µs)	180	2500	75.0%	1.83	6.07	6.50	37.45%
FCS-MPCC (40 µs)	180	2500	75.0%	1.85	5.25	5.56	28.92%
HBVCP-MPCC	180	2500	75.0%	1.85	3.91	4.45	19.80%

Figure 17 briefly illustrates the steady-state operation with a 100 V DC bus voltage, a speed of 500 rpm and two different loads of 2.25 Nm and 4.5 Nm. The corresponding experimental results are demonstrated in Table 3. It can be observed that the HBVCP-MPCC maintains superior current fluctuation, whereas the fluctuation ranges remain nearly the same across different loads. Figure 18 presents the performance of these algorithms under different DC bus voltages with a 4.5 Nm load and 1000 rpm reference speed, and the experimental results are listed in Table 4. These results also validate the relationship in (15).

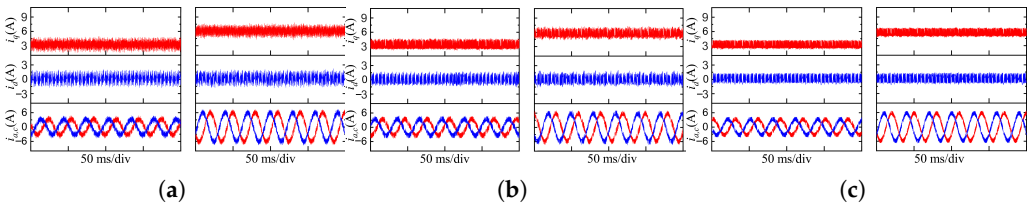
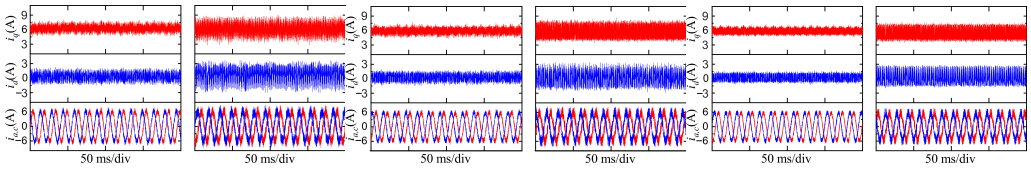


Figure 17. Waveforms with two different load: 2.25 Nm torque load and 4.5 Nm torque load. (**a**) FCS-MPCC with a 76 µs sampling period. (**b**) FCS-MPCC with a 40 µs sampling period. (**c**) HBVCP-MPCC.

Table 3. Steady-state experimental results under different loads ($\omega_r = 500$ rpm, $U_{dc} = 100$ V).

Scheme	T_l/T_N	f_{sw} (kHz)	R_q (A)	R_d (A)
FCS-MPCC (76 µs)	37.5%	2.15	3.16	3.56
FCS-MPCC (40 µs)	37.5%	2.17	2.66	3.18
HBVCP-MPCC	37.5%	2.13	1.97	2.41
FCS-MPCC (76 µs)	75.0%	2.21	3.19	3.58
FCS-MPCC (40 µs)	75.0%	2.23	2.74	3.23
HBVCP-MPCC	75.0%	2.27	2.04	2.37



(**a**) (**b**) (**c**)

Figure 18. Waveforms with two different DC bus voltages: 100 V U_{dc} and 180 V U_{dc}. (**a**) FCS-MPCC with a 76 µs sampling period. (**b**) FCS-MPCC with a 40 µs sampling period. (**c**) HBVCP-MPCC.

Table 4. Steady-state experimental results under different dc bus voltages ($\omega_r = 1000$ rpm, $i_l = 6$ A).

Scheme	U_{dc} (V)	f_{sw} (kHz)	R_q (A)	R_d (A)
FCS-MPCC (76 µs)	100	2.01	3.27	3.57
FCS-MPCC (40 µs)	100	2.00	2.80	3.16
HBVCP-MPCC	100	2.03	2.13	2.52
FCS-MPCC (76 µs)	180	2.27	6.04	6.54
FCS-MPCC (40 µs)	180	2.23	4.71	5.42
HBVCP-MPCC	180	2.29	3.68	4.31

5.2. Dynamic Performance Comparison

The dynamic performance of the proposed method is evaluated under different scenarios. Under a 100 V DC bus voltage, the response to a speed reference step change from 500 rpm to 1000 rpm is shown in Figure 19. Under a 250 V DC bus voltage at 2500 rpm, the response to a load torque step change from 1 Nm to 3 Nm is shown in Figure 20. In both cases, the dynamic adjustment times are comparable across all strategies, attributable to similar speed-loop controllers. A detailed comparison of the q-axis reference current in Figure 21 further confirms that all three schemes achieve similar dynamic performance. The key distinction lies in the current fluctuations: the conventional FCS-MPC exhibits significant current fluctuations, whereas the proposed HBVCP-MPCC maintains smoother currents.

Figure 22 depicts the experimental results when the outer speed loops of all methods are disabled, and the reference of the current in the q-axis is stepped from 1.5 A to 6 A to verify the dynamic performance of the current loops. In this scenario, the motor previously used as a load is set to operate at a fixed speed, making the motor controlled by our algorithm act as the load. The dynamic response capabilities of three schemes are almost the same, and at least in these experiments, no significant differences are detected. However, it can still be observed that the proposed algorithm exhibits the best current performance.

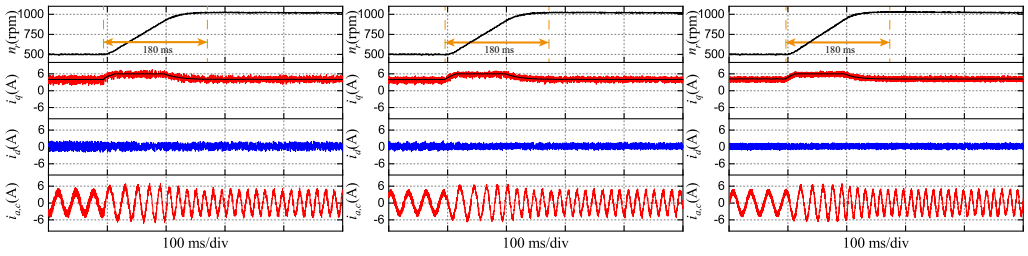


Figure 19. Dynamic experimental waveforms of these control strategies when reference speed step changes from 500 rpm to 1000 rpm: rotating speed, *q*-axis current, *d*-axis current, and phase A current. (**a**) FCS-MPCC with a 76 μs sampling period. (**b**) FCS-MPCC with a 40 μs sampling period. (**c**) HBVCP-MPCC.

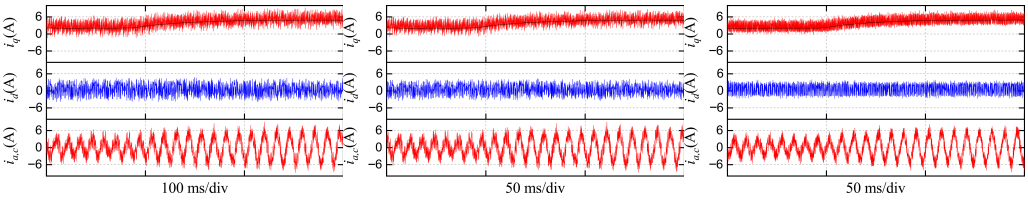


Figure 20. Dynamic experimental waveforms of these control strategies when the torque load step changes from 1 Nm to 3 Nm: *q*-axis current, *d*-axis current, and phase A current. (**a**) FCS-MPCC with a 76 μs sampling period. (**b**) FCS-MPCC with a 40 μs sampling period. (**c**) HBVCP-MPCC.

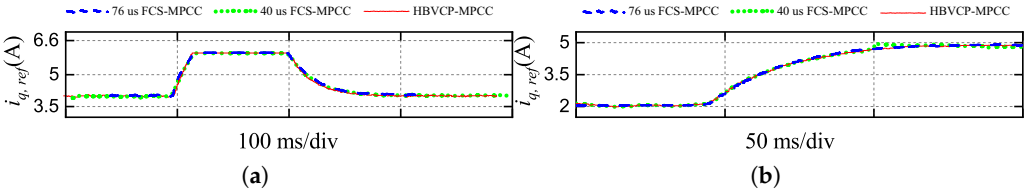


Figure 21. Referencecurrents in the *q*-axis during dynamic experimentation of these control strategies. (**a**) Speed changes. (**b**) Torque changes.

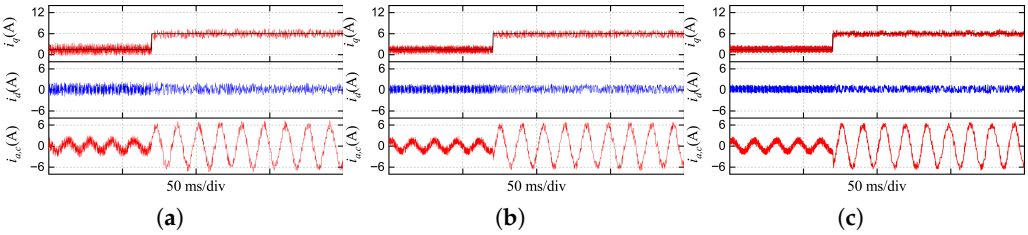


Figure 22. Dynamic experimental waveforms of these control strategies when the reference current in the *q*-axis step changes from 1.5 A to 6 A: *q*-axis current, *d*-axis current, and phase A current. (**a**) FCS-MPCC with a 76 μs sampling period. (**b**) FCS-MPCC with a 40 μs sampling period. (**c**) HBVCP-MPCC.

6. Conclusions

An HBVCP-MPCC method for PMSM drive is proposed in this paper. The digital implementation of the proposed algorithm, including the optimal VV selection, VCP regulation and setting of the current hysteresis width, is described in detail. Benefits from the flexible control period, anticipated benefits in terms of suppressing current fluctuations without increasing switching frequency, are verified with reasonable experiments.

The stable operation of the proposed method under various operating conditions also demonstrates that (1) in non-overmodulation scenarios, the relationship among motor inductances, DC bus voltage, VV action duration range, and hysteresis width can be approximately described by (15); and (2) the approach to seek the optimal VV based on reference voltage is proven effective in experiments.

Author Contributions: Conceptualization, Y.G., F.J., S.W. and S.C.; methodology, Y.G.; software, Y.G. and S.W.; validation, Y.G. and S.C.; formal analysis, Y.G. and S.C.; investigation, Y.G. and S.C.; resources, S.C. and Z.H.; data curation, Y.G., F.J., S.C. and Z.H.; writing—original draft preparation, Y.G.; writing—review and editing, Y.G., F.J., S.W. and S.C.; visualization, Y.G. and F.J.; supervision, S.C. and Z.H.; project administration, S.C. and Z.H. All authors have read and agreed to the published version of the manuscript.

Funding: This research received no external funding.

Institutional Review Board Statement: Not applicable.

Informed Consent Statement: Not applicable.

Data Availability Statement: The data that support the findings of this study are available from the corresponding author upon reasonable request.

Conflicts of Interest: The authors declare no conflicts of interest.

References

1. Fang, S.; Liu, H.; Wang, H.; Yang, H.; Lin, H. High Power Density PMSM With Lightweight Structure and High-Performance Soft Magnetic Alloy Core. *IEEE Trans. Appl. Supercond.* **2019**, *29*, 5. [CrossRef]
2. Kouro, S.; Perez, M.; Rodriguez, J.; Llor, A.; Young, H. Model Predictive Control MPC's Role in the Evolution of Power Electronics. *IEEE Ind. Electron. Mag.* **2015**, *9*, 8–21. [CrossRef]
3. Zhao, Q.; Zhang, Q.; Zhao, S.; Zhang, X.; Lu, S.; Guo, Y.; Song, L.; Zhao, Z. Research on Actuator Control System Based on Improved MPC. *Actuators* **2025**, *14*, 263. [CrossRef]
4. Arahal, M.; Martin, C.; Barrero, F.; Gonzalez-Prieto, I.; Duran, M. Model-Based Control for Power Converters with Variable Sampling Time: A Case Example Using Five-Phase Induction Motor Drives. *IEEE Trans. Ind. Electron.* **2019**, *66*, 5800–5809. [CrossRef]
5. Lin, X.; Liu, J.; Liu, Z.; Gao, Y.; Peretti, L.; Wu, L. Model-Free Current Predictive Control for PMSMs with Ultralocal Model Employing Fixed-Time Observer and Extremum-Seeking Method. *IEEE Trans. Power Electron.* **2025**, *40*, 10682–10693. [CrossRef]
6. Liu, Y.; Cheng, S.; Ning, B.; Li, Y. Robust Model Predictive Control With Simplified Repetitive Control for Electrical Machine Drives. *IEEE Trans. Power Electron.* **2019**, *34*, 4524–4535. [CrossRef]
7. Huang, W.; Hua, W.; Chen, F.; Hu, M.; Zhu, J. Model Predictive Torque Control With SVM for Five-Phase PMSM Under Open-Circuit Fault Condition. *IEEE Trans. Power Electron.* **2020**, *35*, 5531–5540. [CrossRef]
8. Wu, Y.; Zhang, Z.; Yang, Q.; Tian, W.; Karamanakos, P.; Heldwein, M.; Kennel, R. A Direct Model Predictive Control Strategy With an Implicit Modulator for Six-Phase PMSMs. *IEEE J. Emerg. Sel. Top. Power Electron.* **2023**, *11*, 1291–1304. [CrossRef]
9. Xu, R.; Shen, X.; Lin, X.; Liu, Z.; Xu, D.; Liu, J. Robust Model Predictive Control of Position Sensorless-Driven IPMSM Based on Cascaded EKF-LESO. *IEEE Trans. Transp. Electrif.* **2025**, *11*, 8824–8832. [CrossRef]
10. Liu, S.; Liu, C. Virtual-Vector-Based Robust Predictive Current Control for Dual Three-Phase PMSM. *IEEE Trans. Ind. Electron.* **2021**, *68*, 2048–2058. [CrossRef]
11. Saeed, M.; Song, W.; Huang, L.; Yu, B. Double-Vector-Based Finite Control Set Model Predictive Control for Five-Phase PMSMs With High Tracking Accuracy and DC-Link Voltage Utilization. *IEEE Trans. Power Electron.* **2022**, *37*, 15234–15244. [CrossRef]
12. Yang, H.; Li, M.; Zhang, Y.; Xu, A. FCS-MPC for Three-Level NPC Inverter-Fed SPMSM Drives Without Information of Motor Parameters and DC Capacitor. *IEEE Trans. Ind. Electron.* **2024**, *71*, 3504–3513. [CrossRef]
13. Zhang, X.; He, Y. Direct Voltage-Selection Based Model Predictive Direct Speed Control for PMSM Drives Without Weighting Factor. *IEEE Trans. Power Electron.* **2019**, *34*, 7838–7851. [CrossRef]
14. Karamanakos, P.; Geyer, T. Guidelines for the Design of Finite Control Set Model Predictive Controllers. *IEEE Trans. Power Electron.* **2020**, *35*, 7434–7450. [CrossRef]
15. Li, W.; Hang, J.; Ding, S.; Wang, Q. Common Predictive Model for PMSM Drives With Interturn Fault Considering Torque Ripple Suppression. *IEEE Trans. Transp. Electrif.* **2023**, *9*, 4071–4079. [CrossRef]

16. Xie, W.; Wang, X.; Wang, F.; Xu, W.; Kennel, R.; Gerling, D.; Lorenz, R. Finite-Control-Set Model Predictive Torque Control with a Deadbeat Solution for PMSM Drives. *IEEE Trans. Ind. Electron.* **2015**, *62*, 5402–5410. [CrossRef]
17. Hua, C.; Shi, D.; Chen, X.; Gao, G. Ultra-Local Model-Based Adaptive Enhanced Model-Free Control for PMSM Speed Regulation. *Machines* **2025**, *13*, 541. [CrossRef]
18. Xue, Z.; Niu, S.; Li, X. A Simplified Multivector-Based Model Predictive Current Control for PMSM with Enhanced Performance. *IEEE Trans. Transp. Electrif.* **2023**, *9*, 4032–4044. [CrossRef]
19. Meng, Q.; Bao, G. A Novel Low-Complexity Cascaded Model Predictive Control Method for PMSM. *Actuators* **2023**, *12*, 349. [CrossRef]
20. Xu, X.; Tian, H.; Zhang, Z. Dual-Vector Predictive Current Control Strategy for PMSM Based on Voltage Phase Angle Decision and Improved Sliding Mode Controller. *Machines* **2025**, *13*, 767. [CrossRef]
21. Wu, X.; Wang, Y.; Wang, N.; Xing, H.; Xie, W.; Lee, C. A Novel Double-Vector Model-Predictive Current Control for PMSM With Low Computational Burden and Switching Frequency. *IEEE Trans. Power Electron.* **2025**, *40*, 11283–11295. [CrossRef]
22. Petkar, S.; Thippiripati, V. Enhanced Predictive Current Control of PMSM Drive with Virtual Voltage Space Vectors. *IEEE J. Emerg. Sel. Top. Ind. Electron.* **2022**, *3*, 834–844. [CrossRef]
23. Karamanakos, P.; Stolze, P.; Kennel, R.; Manias, S.; Mouton, H. Variable Switching Point Predictive Torque Control of Induction Machines. *IEEE J. Emerg. Sel. Top. Power Electron.* **2014**, *2*, 285–295. [CrossRef]
24. Shi, T.; Xu, Y.; Xiao, M.; Gu, X.; Yan, Y.; Xia, C. VSP predictive torque control of PMSM. *IET Electr. Power Appl.* **2019**, *13*, 463–471. [CrossRef]
25. Song, Z.; Hu, S.; Bao, Z. Variable Action Period Predictive Flux Control Strategy for Permanent Magnet Synchronous Machines. *IEEE Trans. Power Electron.* **2020**, *35*, 6185–6197. [CrossRef]
26. Song, Z.; Cui, Y.; Wang, Y.; Liu, T. Flux-Trajectory-Optimization-Based Predictive Flux Control of Permanent Magnet Synchronous Machines. *IEEE J. Emerg. Sel. Top. Power Electron.* **2021**, *9*, 4364–4375. [CrossRef]
27. Geyer, T.; Papafotiou, G.; Morari, M. Model Predictive Direct Torque Control-Part I: Concept, Algorithm, and Analysis. *IEEE Trans. Ind. Electron.* **2009**, *56*, 1894–1905. [CrossRef]
28. Geyer, T. Model Predictive Direct Current Control Formulation of the stator current bounds and the concept of the switching horizon. *IEEE Ind. Appl. Mag.* **2012**, *18*, 47–59. [CrossRef]
29. Walz, S.; Liserre, M. Hysteresis Model Predictive Current Control for PMSM With LC Filter Considering Different Error Shapes. *IEEE Open J. Power Electron.* **2020**, *1*, 190–197. [CrossRef]
30. Benjamim, W.; Jlassi, I.; Cardoso, A. A Computationally Efficient Model Predictive Current Control of Synchronous Reluctance Motors Based on Hysteresis Comparators. *Electronics* **2022**, *11*, 379. [CrossRef]
31. Dong, Z.; Song, Z.; Wang, W.; Liu, C. Improved Zero-Sequence Current Hysteresis Control-Based Space Vector Modulation for Open-End Winding PMSM Drives With Common DC Bus. *IEEE Trans. Ind. Electron.* **2023**, *70*, 10755–10760. [CrossRef]

Disclaimer/Publisher's Note: The statements, opinions and data contained in all publications are solely those of the individual author(s) and contributor(s) and not of MDPI and/or the editor(s). MDPI and/or the editor(s) disclaim responsibility for any injury to people or property resulting from any ideas, methods, instructions or products referred to in the content.